A&A 508, 501–511 (2009)
DOI: 10.1051/0004-6361/200913082
© ESO 2009

Astronomy & Astrophysics

Benchmarking atomic data for astrophysics: Fe VII and other cool lines observed by Hinode EIS

G. Del Zanna

DAMTP, Centre for Mathematical Sciences, Wilberforce road Cambridge CB3 0WA, UK
e-mail: GDelZanna@spd.aas.org

Received 7 August 2009 / Accepted 11 September 2009

ABSTRACT

The EUV spectrum of Fe VII is reviewed, using new rates for electron impact excitation, atomic structure calculations, and experimental data. In particular, solar observations of a sunspot loop spectrum obtained from the Hinode EUV Imaging Spectrometer (EIS) are used. Previous line identifications, mostly based on laboratory data, have been assessed. Large discrepancies between observed and predicted line intensities and wavelengths are found for the decays from the $3s^2\ 3p^5\ 3d^3$ configuration, which are strong EUV lines. We ascribe these discrepancies to incorrect line identifications. A number of new identifications are proposed. With these, very good agreement between theory and experimental data is found. A few transitions, in particular from the $3s^2\ 3p^6\ 3d\ 4s$ configuration, are observed for the first time, and are shown to provide a new important diagnostic for measuring the electron temperature in the solar transition region. The temperatures obtained at the base of solar coronal loops are found to be close to the temperature of maximum abundance in ionization equilibrium ($\log T[\mathrm{K}] = 5.4$). The assessment of the Fe VII lines was done in conjunction with an assessment of all the strongest cool lines observed with EIS. This spectrum is rich in transition region lines. Some new identifications are presented, in particular for Fe IX. Most of the strongest transitions are identified, however a large number of lines still awaits firm identification.

Key words. atomic data – line: identification – Sun: transition region – techniques: spectroscopic

1. Introduction

This paper is one in a series where atomic data and line identifications are benchmarked against experimental data (Del Zanna et al. 2004, Paper I). A substantial amount of work has been devoted in the literature to the study of the visible and UV transitions of Fe VII, however little has been done on the EUV spectrum. Witthoeft & Badnell (2008, hereafter WB08) have recently performed a large electron scattering calculation for this ion as part of the Iron Project and the UK Rmax network (now superseded by the UK APAP network). For a description of previous work on electron impact excitation for this ion see WB08. The new rates, together with the new accurate Hinode EUV Imaging Spectrometer (EIS, see Culhane et al. 2007) observations, provide the opportunity to study in detail many of the strongest lines in the EUV spectrum of Fe VII. The aim of this paper is to reassess previous identifications, and suggest which lines are best for diagnostic purposes. This paper complements a similar paper (Del Zanna 2009) where the EUV spectrum of Fe VIII is discussed, using the same EIS observation.

In this paper, we focus on the $n = 3, 4$ lower configurations which produce the strong EUV transitions. Contrary to many other ions, very little experimental work has been done on Fe VII EUV lines. The identification of Fe VII EUV lines started with Fawcett & Cowan (1973, hereafter FC73), who identified five among the strongest transitions from the $3s^2\ 3p^5\ 3d^3$ configuration, using a laboratory vacuum spark spectrum and atomic structure calculations. Ekberg (1981, hereafter E81) also used a vacuum spark source and Hartree-Fock calculations to identify an impressively large (more than 400) number of lines, and many levels, in particular of the $3s^2\ 3p^5\ 3d^3$ and $3s^2\ 3p^6\ 3d\ 4p$ configurations. A number of UV lines were also identified. Later, levels of the $3s^2\ 3p^6\ 3d\ 4d$ configuration were identified by Ekberg & Feldman (2003) using UV lines in a very nice piece of work.

To date, Ekberg's is the only work on the Fe VII EUV lines. Wavelengths were very accurate, to within a few m Å. The original spectra, which contained large numbers of lines, were not published, so for a number of cases it has not been possible to confirm identifications. The spectra contained lines from nearby ionization stages, so it is always possible that some of the lines identified by E81 were not due to Fe VII. Most level energies were obtained from various wavelength coincidences among decays to the levels of the ground configuration, which have been known with high accuracy, so at first it seemed that all of Ekberg's identifications must have been correct.

However, the benchmark iterative procedure has highlighted a number of problems with Ekberg's work. First, it turns out that a number of lines among those with largest gf values were not identified. This includes the line with by far the largest value. Second, for a number of levels, observed energies are very far from those predicted theoretically, based on level splittings. Third, for some levels, deviations from the ab-initio calculated energies are unreasonably large. A detailed assessment for each of the strongest spectral lines had to be done, and is described below. A number of new identifications are presented, while a number of uncertain ones are also suggested.

The assessment of the Fe VII lines was done in conjunction with an assessment of all the strongest transition region (TR) lines observed with EIS, which is also presented in this paper.

Article published by EDP Sciences

2. Atomic structure for Fe VII

As for Fe VIII, it is particularly difficult to obtain ab-initio level energies that match the observed ones for this ion. Configuration-interaction (CI) and mixing effects are also large, as described in WB08. For these reason, it has been particularly difficult to obtain firm identifications for Fe VII. Relativistic multi-reference many-body perturbation theory calculations such as those described in Ishikawa & Vilkas (2008) are needed, since they have been proved to provide very good level energies. Also, new experimental data would be useful to confirm the identifications proposed here.

Fortunately, mixing effects turn out to be not as important as it was the case for Fe VIII (Del Zanna 2009). This has been assessed by running various atomic structure calculations using the AUTOSTRUCTURE code (Badnell 1997). A basis which reproduced well all the levels from the main spectroscopically-important configurations could not be found. As a "benchmark" structure calculation, we chose the large 40-configuration basis described by WB08, with the same scaling parameters. To improve the level energies, term energy corrections (TEC) (see, e.g. Zeippen et al. 1977; Nussbaumer & Storey 1978) to the *LS* Hamiltonian matrix were applied, using the iterative procedure described in Paper I.

The corrections to the *LS* term energies were estimated from the weighted mean of the observed level energies, whenever available. Most TEC values for the important $3d^3$ configuration were only about 13 000 cm^{-1}, so this correction has been applied to all the *LS* terms from this configuration for which no experimental energies were available. The energies of this benchmark calculation ($E_{\rm Bench.}$) are shown in Table 1. They are to be compared to the new experimental energies presented here ($E_{\rm Exp.}$), together with those from the scattering calculation and those from the NIST database[1], which are derived from Ekberg's work for the $3s^2\ 3p^6\ 3d\ 4s$, $3s^2\ 3p^5\ 3d^3$ configurations. The TEC iterative method has been essential to establish which spectral lines had correct identifications and which did not. Also, it has been used as a check for the validity of the scattering target. The target basis chosen by WB08 turns out to be quite accurate, given the complexity of this ion. In particular, the relative energies between strongly-mixed levels are close to the observed ones. This is reflected by the oscillator strengths. This is reassuring, and confirms the accuracy of the target adopted by WB08. Table 2 lists the weighted oscillator strengths (gf) for the strongest dipole-allowed transitions, compared to the WB08 values.

Line intensities were calculated with the WB08 rates and the transition probabilities from the benchmark (+TEC) calculation (adopting the WB08 probabilities changes the intensities by only up to 10%). We assumed plasma equilibrium conditions, and an electron density of 10^9 cm^{-3}, typical for loop legs (Del Zanna & Mason 2003). The line intensities, listed in Table 2 in decreasing order, were calculated at the temperature $\log T[\mathrm{K}] = 5.4$. This is the temperature of peak ion abundance for Fe VII in ionization equilibrium, according to the latest ionization and recombination rates published within CHIANTI[2] v.6 (Dere et al. 1997, 2009).

All the identifications of the strongest lines have been checked, using laboratory and solar spectra, as described in the following Section. Line intensities, whenever available, were compared, in order to confirm identifications and assess the possible presence of blending. The results are also shown in Table 2.

[1] http://physics.nist.gov/PhysRefData/ASD/index.html
[2] www.chianti.rl.ac.uk

3. Experimental data

One of the original plates from B.C.Fawcett was found to contain strong transition region lines, mostly from Fe VIII, Fe IX. The plate was scanned, and an averaged spectrum wavelength-calibrated. Lines from different ionization stages of Iron are present, as well as other C, O lines. This spectrum was used as an aid in the identification process, in particular for the wavelengths not observed by Hinode EIS. All the Fe VII lines with large gf values observed by EIS and by E81 were also observed in this spectrum. The E81 and Hinode EIS wavelengths are far more accurate than those of this spectrum, so they have been used. In a few cases, new tentative identifications based on this plate are proposed (see Table 2 for the spectroscopic identification). The firm identifications proposed here are based on the Hinode/EIS data, in particular on morphology, line intensity and wavelength.

The Hinode/EIS instrument covers two wavelength bands (SW: 166−212 Å; LW: 245−291 Å). Here we consider a long-exposure (90 s) observation which started on 2007 Jan. 5 at 21:52 UT and observed a sunspot and various loops. A complex data processing, which included various geometrical corrections and a wavelength calibration procedure was applied to the data, as described in detail in Del Zanna (2009). More than 200 lines were fitted with Gaussian profiles using the *cfit* package (Haugan 1997), and their morphology examined in detail, one by one.

Figure 1 shows the resulting monochromatic images for a selection of Fe VII and other lines, to show how sensitive morphology is to the different ion stages. This allows to estimate the temperature of formation for the strongest unidentified lines, and to assess if/when Fe VII lines are blended.

A spectrum over an area in a sunspot loop leg was chosen for the benchmark. The area is indicated by the crossing of the two sets of dashed lines in Fig. 2. A "foreground" spectrum was subtracted, to remove the small contribution from coronal lines. The resultant spectrum has a wavelength uncertainty of about 5 m Å and very strong cool lines. The little coronal contamination inside the sunspot, and the foreground subtraction means that each feature in this spectrum can only be produced by a spectral line formed at transition-region temperatures. The only high-T residual emission is from Fe X, which is formed around 1 MK. Lines formed above 1 MK are not present. A sample of spectral windows from the sunspot loop and the foreground spectrum is provided in Fig. 3.

Table 3 provides the list of the strongest lines present in this spectrum, with their measured wavelengths $\lambda_{\rm o}$ and intensities. Notice that both the intensities in terms of total counts in the lines are given, as well as the calibrated ones. This was done to highlight the fact that many intrinsically-weak spectral lines which fall near the peak sensitivity of the channels do actually have large count rates.

As shown in Del Zanna (2007, 2008), the legs of active regions loops present strong red-shifts, increasingly larger for lines formed at lower temperatures. The pattern is clearly shown in Fig. 2. The sunspot leg area selected presents a red-shift of about 20 $km\,s^{-1}$ in lines from Fe VIII, Si VII, Mg VII (Del Zanna 2009), while lines from Fe VII, Si VI, Mg VI are red-shifted by about 30 $km\,s^{-1}$, as shown in Fig. 2. Lines from higher-T such as those from Fe IX were red-shifted by only 10 $km\,s^{-1}$, while those at lower T by about 35 $km\,s^{-1}$. The corrections for these red-shifts have been applied to the measured $\lambda_{\rm o}$ to obtain the "rest" wavelengths $\lambda_{\rm c}$ (Å), also shown in Table 3. This was done in all cases when a line had an established formation temperature. The overall cumulative uncertainty on the $\lambda_{\rm c}$ values is

Table 1. Level energies for Fe VII.

i	Conf.	Lev.	$E_{\rm exp}$	$E_{\rm Bench.}$	$E_{\rm NIST}$	$E_{\rm WB08}$
1	$3s^2\ 3p^6\ 3d^2$	$^3F_2$	0.0	0.0	0.0 (0)	0.0 (0)
2	$3s^2\ 3p^6\ 3d^2$	$^3F_3$	1051.5	1192.0 (140.5)	1051.5 (0)	1280.0 (–229)
3	$3s^2\ 3p^6\ 3d^2$	$^3F_4$	2331.5	2635.0 (303.5)	2331.5 (0)	2856.0 (–525)
4	$3s^2\ 3p^6\ 3d^2$	$^1D_2$	17 475.5	17 436.0 (39.5)	17 475.5 (0)	18 269.0 (–794)
5	$3s^2\ 3p^6\ 3d^2$	$^3P_0$	20 040.3	19 949.0 (91.3)	20 040.3 (0)	21 313.0 (–1273)
6	$3s^2\ 3p^6\ 3d^2$	$^3P_1$	20 430.1	20 389.0 (41.1)	20 430.1 (0)	21 782.0 (–1352)
7	$3s^2\ 3p^6\ 3d^2$	$^3P_2$	21 278.6	21 373.0 (−94.4)	21 278.6 (0)	22 869.0 (–1590)
8	$3s^2\ 3p^6\ 3d^2$	$^1G_4$	28 927.3	28 933.0 (−5.7)	28 927.3 (0)	32 504.0 (–3577)
9	$3s^2\ 3p^6\ 3d^2$	$^1S_0$	67 078.3	67 081.0 (−2.7)	67 078.3 (0)	67 906.0 (–828)
10	$3s^2\ 3p^6\ 3d\ 4s$	$^3D_1$	344 463.3	344 398.0 (65.3)	344 463.3 (0)	341 232.0 (3231)
11	$3s^2\ 3p^6\ 3d\ 4s$	$^3D_2$	345 028.7	344 990.0 (38.7)	345 028.7 (0)	341 875.0 (3154)
12	$3s^2\ 3p^6\ 3d\ 4s$	$^3D_3$	346 262.2	346 310.0 (−47.8)	346 262.2 (0)	343 256.0 (3006)
13	$3s^2\ 3p^6\ 3d\ 4s$	$^1D_2$	350 332.6	350 355.0 (−22.4)	350 332.6 (0)	347 957.0 (2376)
19	$3s^2\ 3p^5\ 3d^3$	$^5D_4$	385 950.0	386 026.0 (−76.0)	–	399 401.0 (–13 451)
20	$3s^2\ 3p^5\ 3d^3$	$^5F_5$	395 953.0	395 927.0 (26.0)	–	408 229.0 (–12 276)
22	$3s^2\ 3p^5\ 3d^3$	$^5F_4$	396 778	396 783.0 (−5)	–	409 084.0 (–12 306)
25	$3s^2\ 3p^6\ 3d\ 4p$	$^1D_2$	425 386.1	426 421.0 (−1034.9)	425 386.1 (0)	421 304.0 (4082)
27	$3s^2\ 3p^6\ 3d\ 4p$	$^3D_1$	425 128.6	429 121.0 (−3992.4)	425 128.6 (0)	422 621.0 (2508)
28	$3s^2\ 3p^6\ 3d\ 4p$	$^3D_2$	427 784.7	430 017.0 (−2232.3)	427 784.7 (0)	423 676.0 (4109)
30	$3s^2\ 3p^5\ 3d^3$	$^3D_2$	411 173.0	416 090.0 (−4917.0)	–	424 125.0 (–12 952)
31	$3s^2\ 3p^6\ 3d\ 4p$	$^3D_3$	430 948.6	430 850.0 (98.6)	430 948.6 (0)	424 636.0 (6313)
32	$3s^2\ 3p^6\ 3d\ 4p$	$^3F_3$	431 609.5	432 222.0 (−612.5)	431 609.5 (0)	425 799.0 (5811)
35	$3s^2\ 3p^6\ 3d\ 4p$	$^3F_2$	430 213.4	430 455.0 (−241.6)	430 213.4 (0)	427 600.0 (2613)
36	$3s^2\ 3p^6\ 3d\ 4p$	$^3F_4$	433 871.2	433 727.0 (144.2)	433 871.2 (0)	428 464.0 (5407)
37	$3s^2\ 3p^5\ 3d^3$	$^3F_2$	414 901.0	418 828.0 (−3927.0)	–	431 058.0 (–16 157)
44	$3s^2\ 3p^6\ 3d\ 4p$	$^3P_2$	437 558.0	436 964.0 (594.0)	437 558.0 (0)	434 356.0 (3202)
46	$3s^2\ 3p^6\ 3d\ 4p$	$^1F_3$	439 811.6	439 825.0 (−13.4)	439 811.6 (0)	437 964.0 (1848)
51	$3s^2\ 3p^5\ 3d^3$	$^3G_4$	426 258.0	426 222.0 (36.0)	–	439 690.0 (–13 432)
52	$3s^2\ 3p^5\ 3d^3$	$^3G_5$	426 726.0	426 664.0 (62.0)	–	440 009.0 (–13 283)
53	$3s^2\ 3p^6\ 3d\ 4p$	$^1P_1$	443 447.0	443 499.0 (−52.0)	443 447.0 (0)	442 075.0 (1372)
93	$3s^2\ 3p^5\ 3d^3$	$^3H_5$	472 557.0	470 937.0 (1620.0)	464 034.0 (8523)	484 884.0 (–12 327)
97	$3s^2\ 3p^5\ 3d^3$	$^3G_5$	479 133.0	477 496.0 (1637.0)	472 559.0 (6574)	491 478.0 (–12 345)
98	$3s^2\ 3p^5\ 3d^3$	$^3G_4$	479 926.0	478 478.0 (1448.0)	472 903.0 (7023)	492 013.0 (–12 087)
101	$3s^2\ 3p^5\ 3d^3$	$^3G_3$	483 667.0	481 477.0 (2190.0)	481 435.0 (2232)	495 023.0 (–11 356)
104	$3s^2\ 3p^5\ 3d^3$	$^1G_4$	496 454.0	496 425.0 (29.0)	496 454.0 (0)	509 993.0 (–13 539)
106	$3s^2\ 3p^5\ 3d^3$	$^3G_3$	506 693.0	507 719.0 (−1026.0)	510 086.0 (–3393)	524 582.0 (–17 889)
108	$3s^2\ 3p^5\ 3d^3$	$^3G_4$	510 709.0	510 971.0 (−262.0)	510 158.0 (551)	527 664.0 (–16 955)
110	$3s^2\ 3p^5\ 3d^3$	$^3G_5$	512 415.0	512 497.0 (−82.0)	514 133.0 (–1718)	529 895.0 (–17 480)
115	$3s^2\ 3p^5\ 3d^3$	$^1D_2$	538 290.0	538 356.0 (−66.0)	538 290.0 (0)	554 792.0 (–16 502)
116	$3s^2\ 3p^5\ 3d^3$	$^1H_5$	538 588.0	538 571.0 (17.0)	–	556 628.0 (–18 040)
118	$3s^2\ 3p^5\ 3d^3$	$^3D_2$	551 864.0	551 784.0 (80.0)	548 274.0 (3590)	569 214.0 (–17 350)
119	$3s^2\ 3p^5\ 3d^3$	$^3D_3$	552 658.0	552 763.0 (−105.0)	556 422.0 (–3764)	570 068.0 (–17 410)
120	$3s^2\ 3p^5\ 3d^3$	$^1F_3$	557 184.0	557 281.0 (−97.0)	551 568.0 (5616)	574 639.0 (–17 455)
121	$3s^2\ 3p^5\ 3d^3$	$^1D_2$	561 477.0	560 937.0 (540.0)	553 220.0 (8257)	575 312.0 (–13 835)
130	$3s^2\ 3p^5\ 3d^3$	$^3P_1$	–	565 973.0	561 303.0	583 752.0
131	$3s^2\ 3p^5\ 3d^3$	$^3F_2$	564 425.0	564 784.0 (−359.0)	564 425.0 (0)	583 775.0 (–19 350)
133	$3s^2\ 3p^5\ 3d^3$	$^3F_3$	566 256.0	566 261.0 (−5.0)	566 256.0 (0)	585 593.0 (–19 337)
134	$3s^2\ 3p^5\ 3d^3$	$^3P_2$	570 327.0	569 856.0 (471.0)	565 275.0 (5052)	587 593.0 (–17 266)
135	$3s^2\ 3p^5\ 3d^3$	$^3F_4$	568 118.0	568 202.0 (−84.0)	568 118.0 (0)	587 711.0 (–19 593)
146	$3s^2\ 3p^5\ 3d^3$	$^1P_1$	598 638.0	598 666.0 (−28.0)	598 638.0 (0)	619 606.0 (–20 968)
147	$3s^2\ 3p^5\ 3d^3$	$^3D_2$	603 757.0	603 603.0 (154.0)	603 757.0 (0)	624 084.0 (–20 327)
148	$3s^2\ 3p^5\ 3d^3$	$^3D_3$	603 419.0	603 665.0 (−246.0)	603 419.0 (0)	624 266.0 (–20 847)
149	$3s^2\ 3p^5\ 3d^3$	$^3D_1$	604 270.0	603 991.0 (279.0)	604 270.0 (0)	624 486.0 (–20 216)
150	$3s^2\ 3p^5\ 3d^3$	$^1G_4$	613 483.0	613 387.0 (96.0)	605 489.0 (7994)	625 447.0 (–11 964)
151	$3s^2\ 3p^5\ 3d^3$	$^3S_1$	623 699.0	623 696.0 (3.0)	623 699.0 (0)	640 135.0 (–16 436)
152	$3s^2\ 3p^5\ 3d^3$	$^1P_1$	630 283.0	630 291.0 (−8.0)	630 283.0 (0)	647 721.0 (–17 438)
153	$3s^2\ 3p^5\ 3d^3$	$^1F_3$	634 668	637 421.0 (−2753)	–	654 512.0 (–19 844)

Note: the first three columns indicate the indices (following the level ordering of WB08), the configuration and dominant *LS J*. The following columns list the experimental level energies $E_{\rm exp}$ (cm^{-1}), those obtained from the benchmark calculation $E_{\rm Bench.}$, those from NIST v.3 and those of the WB08 scattering target $E_{\rm WB08}$. Values in parentheses indicate differences with the experimental energies. Only a selection of observed levels from the lower configurations, producing the EUV lines discussed here, are presented.

Table 2. List of the strongest Fe VII EUV lines in the 160–295 Å range.

$i-j$	Levels	Int	gf	gf^*	$A_{ji}(s^{-1})$	λ_{exp}(Å)	λ_{th}(Å)	λ_{NIST}(Å)	ID
3–135	$3d^2\ ^3F_4$–$3d^3\ ^3F_4$	1.0	7.15	7.4	1.7×10^{11}	176.745	176.81	176.745	FC73
3–148	$3d^2\ ^3F_4$–$3d^3\ ^3D_3$	0.78	8.55	8.8	2.9×10^{11}	166.365	166.38	166.365	FC73
3–110	$3d^2\ ^3F_4$–$3d^3\ ^3G_5$	0.86	2.90	3.0	4.6×10^{10}	196.046	196.13	195.388	N
8–150	$3d^2\ ^1G_4$–$3d^3\ ^1G_4$	0.73	8.52	8.6	2.2×10^{11}	171.070	171.10	173.442	T N
2–133	$3d^2\ ^3F_3$–$3d^3\ ^3F_3$	0.71	5.03	5.2	1.5×10^{11}	176.927	176.97	176.927	FC73
8–153	$3d^2\ ^1G_4$–$3d^3\ ^1F_3$	0.61	9.82	10.	3.5×10^{11}	165.087	164.34	–	T N
2–147	$3d^2\ ^3F_3$–$3d^3\ ^3D_2$	0.53	5.85	6.0	2.8×10^{11}	165.919	166.00	165.919	FC73
2–108	$3d^2\ ^3F_3$–$3d^3\ ^3G_4$	0.61	1.24	2.1	2.4×10^{10}	196.210	196.16	196.423	N
1–131	$3d^2\ ^3F_2$–$3d^3\ ^3F_2$	0.47	3.19	3.8	1.4×10^{11}	177.171	177.06	177.171	FC73
8–116	$3d^2\ ^1G_4$–$3d^3\ ^1H_5$	0.47	2.22	2.3	3.5×10^{10}	196.209	196.22	–	N
7–120	$3d^2\ ^3P_2$–$3d^3\ ^1F_3$	0.34	2.00	2.3	5.5×10^{10}	186.600	186.60	188.576	N
1–149	$3d^2\ ^3F_2$–$3d^3\ ^3D_1$	0.30	3.44	3.5	2.8×10^{11}	165.489	165.57	165.489	E81
4–119	$3d^2\ ^1D_2$–$3d^3\ ^3D_3$	0.34	2.01	2.3	5.5×10^{10}	186.852	186.80	185.547	N
7–134	$3d^2\ ^3P_2$–$3d^3\ ^3P_2$	0.32	2.26	2.3	9.1×10^{10}	182.133	182.32	183.825	N
4–121	$3d^2\ ^1D_2$–$3d^3\ ^1D_2$	0.32	2.24	2.3	8.8×10^{10}	183.823	183.99	186.656	N
1–106	$3d^2\ ^3F_2$–$3d^3\ ^3G_3$	0.33	1.36	1.1	3.3×10^{10}	197.358	196.96	196.045	N
2–98	$3d^2\ ^3F_3$–$3d^3\ ^3G_4$	0.35	0.73	0.74	1.2×10^{10}	208.823	209.52	211.931	N
3–97	$3d^2\ ^3F_4$–$3d^3\ ^3G_5$	0.34	0.62	0.60	8.5×10^{9}	209.731	210.59	212.663	N
3–43	$3d^2\ ^3F_4$–$3d^3\ ^3F_4$	0.35	6.2×10^{-2}	0.13	8.0×10^{8}	–	239.24	–	
3–52	$3d^2\ ^3F_4$–$3d^3\ ^3G_5$	0.31	9.2×10^{-2}	9.5×10^{-2}	1.0×10^{9}	235.630	235.83	–	T N
3–20	$3d^2\ ^3F_4$–$3d^3\ ^5F_5$	0.34	1.7×10^{-5}	1.4×10^{-5}	1.6×10^{5}	254.051	254.26	–	N
3–19	$3d^2\ ^3F_4$–$3d^3\ ^5D_4$	0.29	8.5×10^{-4}	2.9×10^{-4}	9.3×10^{6}	260.676	260.83	–	N
1–101	$3d^2\ ^3F_2$–$3d^3\ ^3G_3$	0.31	0.75	0.75	1.7×10^{10}	206.754	207.69	207.712	N
1–37	$3d^2\ ^3F_2$–$3d^3\ ^3F_2$	0.26	2.1×10^{-2}	8.7×10^{-4}	4.8×10^{8}	241.021	238.76	–	T N
2–42	$3d^2\ ^3F_3$–$3d^3\ ^3F_3$	0.23	3.7×10^{-2}	1.8×10^{-3}	6.2×10^{8}	–	239.53	–	
3–29	$3d^2\ ^3F_4$–$3d^3\ ^5G_5$	0.24	5.2×10^{-5}	7.4×10^{-5}	5.2×10^{5}	–	245.00	–	
2–51	$3d^2\ ^3F_3$–$3d^3\ ^3G_4$	0.23	0.11	9.0×10^{-2}	1.5×10^{9}	235.180	235.28	–	T N
2–30	$3d^2\ ^3F_3$–$3d^3\ ^3D_2$	0.22	4.1×10^{-2}	0.16	9.4×10^{8}	243.830	241.02	–	T N
3–22	$3d^2\ ^3F_4$–$3d^3\ ^5F_4$	0.22	1.0×10^{-3}	2.0×10^{-4}	1.2×10^{7}	253.520	253.71	–	T N
6–118	$3d^2\ ^3P_1$–$3d^3\ ^3D_2$	0.24	1.35	1.2	5.1×10^{10}	188.170	188.18	189.450	N
4–152	$3d^2\ ^1D_2$–$3d^3\ ^1P_1$	0.18	2.84	3.0	2.4×10^{11}	163.183	163.17	163.183	E81
7–151	$3d^2\ ^3P_2$–$3d^3\ ^3S_1$	0.17	2.30	2.4	1.9×10^{11}	165.997	166.02	165.997	E81
3–93	$3d^2\ ^3F_4$–$3d^3\ ^3H_5$	0.20	0.16	0.28	2.1×10^{9}	212.664	213.54	216.590	T N
4–120	$3d^2\ ^1D_2$–$3d^3\ ^1F_3$	0.14	0.78	0.56	2.2×10^{10}	185.285	185.24	187.233	N
6–151	$3d^2\ ^3P_1$–$3d^3\ ^3S_1$	0.11	1.49	1.5	1.2×10^{11}	165.764	165.75	165.764	E81
7–119	$3d^2\ ^3P_2$–$3d^3\ ^3D_3$	0.12	0.73	0.52	2.0×10^{10}	188.189	188.19	186.866	N
8–46	$3d^2\ ^1G_4$–$4p\ ^1F_3$	1.2	1.71	1.7	2.8×10^{10}	243.378	243.37	243.378	E81
3–31	$3d^2\ ^3F_4$–$4p\ ^3D_3$	0.78	0.90	0.80	1.6×10^{10}	233.308	233.53	233.308	E81
3–36	$3d^2\ ^3F_4$–$4p\ ^3F_4$	0.70	0.48	0.46	6.6×10^{9}	231.728	231.97	231.728	E81
4–25	$3d^2\ ^1D_2$–$4p\ ^1D_2$	0.59	0.37	0.39	8.3×10^{9}	245.152	244.51	245.152	E81
2–28	$3d^2\ ^3F_3$–$4p\ ^3D_2$	0.48	0.46	0.59	1.1×10^{10}	234.338	233.20	234.338	E81
1–27	$3d^2\ ^3F_2$–$4p\ ^3D_1$	0.46	0.45	0.51	1.9×10^{10}	235.223	233.04	235.223	E81
7–44	$3d^2\ ^3P_2$–$4p\ ^3P_2$	0.33	0.54	0.32	1.2×10^{10}	240.223	240.62	240.223	E81
3–32	$3d^2\ ^3F_4$–$4p\ ^3F_3$	0.28	0.27	0.25	4.7×10^{9}	232.949	232.78	232.949	E81
4–53	$3d^2\ ^1D_2$–$4p\ ^1P_1$	0.25	0.29	0.30	1.2×10^{10}	234.757	234.71	234.757	E81
2–32	$3d^2\ ^3F_3$–$4p\ ^3F_3$	0.24	0.23	0.11	4.1×10^{9}	232.257	232.00	232.257	E81
2–35	$3d^2\ ^3F_3$–$4p\ ^3F_2$	0.23	0.29	1.8×10^{-2}	7.1×10^{9}	233.012	232.96	233.012	E81
1–28	$3d^2\ ^3F_2$–$4p\ ^3D_2$	0.20	0.19	0.12	4.7×10^{9}	233.762	232.55	233.762	E81
2–31	$3d^2\ ^3F_3$–$4p\ ^3D_3$	0.19	0.22	0.21	3.9×10^{9}	232.614	232.74	232.614	E81
3–12	$3d^2\ ^3F_4$–$4s\ ^3D_3$	1.3	–	–	1.6×10^{5}	290.756	290.97	290.756	N
2–11	$3d^2\ ^3F_3$–$4s\ ^3D_2$	0.61	–	–	1.0×10^{5}	290.717	290.87	290.717	N
1–10	$3d^2\ ^3F_2$–$4s\ ^3D_1$	0.53	–	–	1.4×10^{5}	290.307	290.36	290.307	N
1–11	$3d^2\ ^3F_2$–$4s\ ^3D_2$	0.37	–	–	6.2×10^{4}	289.831	289.86	289.831	N
2–12	$3d^2\ ^3F_3$–$4s\ ^3D_3$	0.37	–	–	4.6×10^{4}	289.678	289.76	289.678	N
3-11	$3d^2\ ^3F_4$–$4s\ ^3D_2$	0.27	–	–	4.5×10^{4}	291.803	292.09	291.803	N
2–10	$3d^2\ ^3F_3$–$4s\ ^3D_1$	0.26	–	–	7.1×10^{4}	291.196	291.37	291.196	N

Note: the relative intensities (photons) Int $= N_j A_{ji}/N_e$ are normalised to the strongest transition and were calculated at an electron density of 10^9 cm^{-3} and a temperature of 2.5×10^5 K. Weighted oscillator strengths gf and A-values (s^{-1}) are from the benchmark calculation. The gf values from WB08 are also listed (gf^*). λ_{exp} are our experimental wavelengths, while λ_{th} are the theoretical ones from the benchmark calculation. λ_{NIST} are the NIST wavelengths. The last column (ID) provides a key to previous identifications. N indicates a new one proposed here. T N a tentative new one. FC73: Fawcett & Cowan (1973); E81: Ekberg (1981).

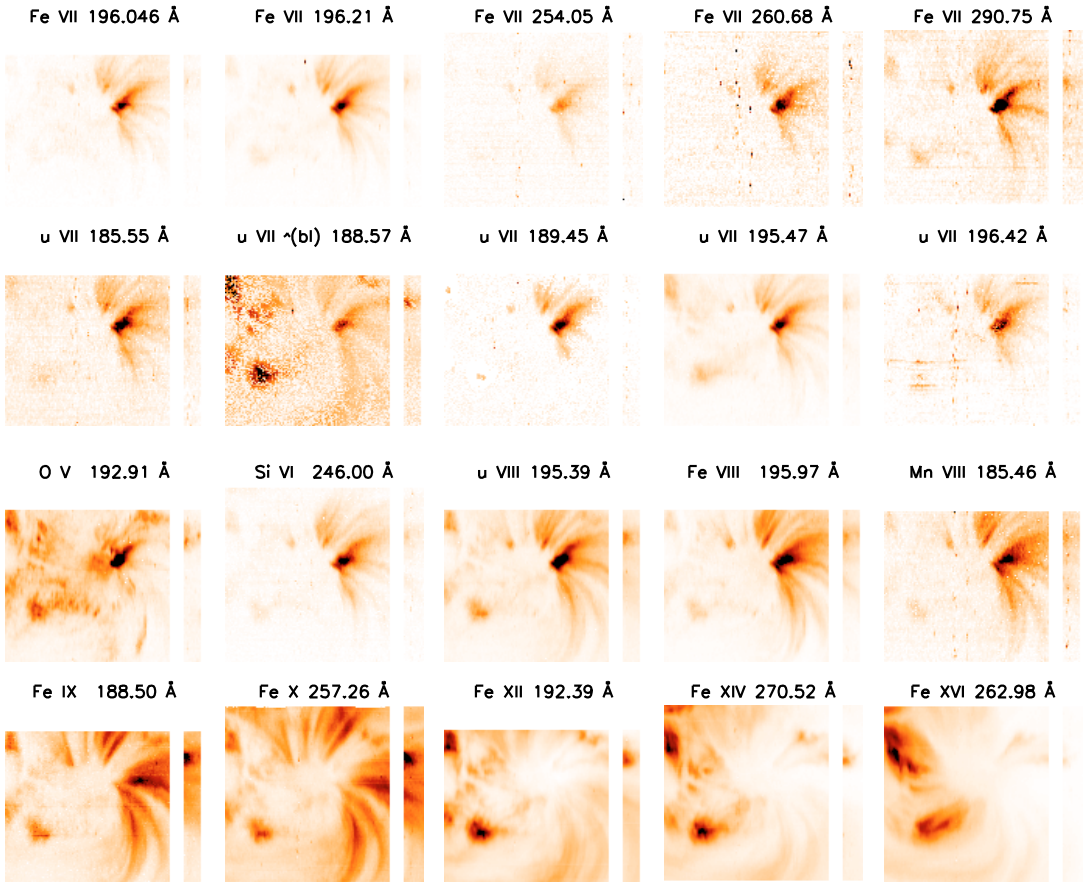

Fig. 1. *Top*: monochromatic images (negative) of the strongest Fe VII lines observed by EIS. Notice that all the Fe VII lines have a similar morphology. Also displayed are a few lines which have the same morphology as Fe VII but are considered as unidentified (u VII). A few lines formed over a range of temperatures are also displayed.

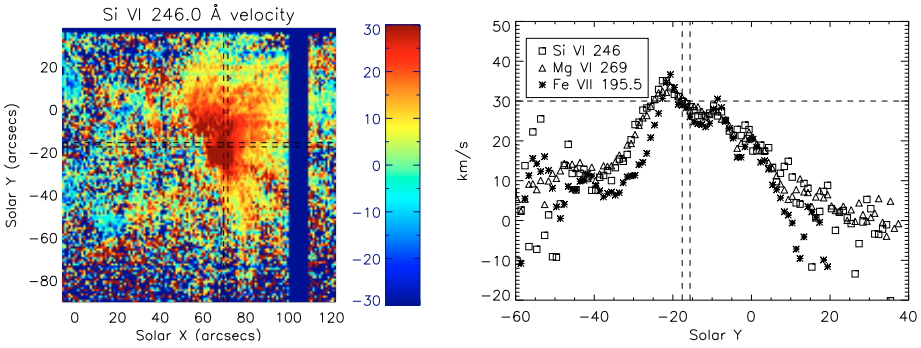

Fig. 2. *Left*: doppler-gram of the Si VI 246.0 Å line showing strong (30 km s^{-1}) red-shifts in the legs of a fan of coronal loops anchored in a sunspot. The location of the area chosen to obtain averaged spectra from a sunspot loop leg is indicated by the crossing of the two sets of dashed lines. *Right*: doppler-shifts in a few lines formed at similar temperatures, along the N-S direction indicated by the dashed lines in the *left figure*. At the location of the loop leg, all lines are red-shifted by about 30 km s^{-1}.

estimated to be about 5 m Å. Many values are within a few m Å from the literature values, also shown in Table 3. This agreement is remarkable. The table also clearly indicates that a considerable number of rest wavelengths, in particular for Si VII, need to be revised.

4. Fe VII line identifications

For the line identification, we make use of the "emissivity ratio" technique, whereby the observed intensity of a line is divided by its emissivity (as a function of electron temperature or density) and by a normalization factor. This allows, in one single plot, to assess at once for a group of lines how good observed vs. theoretical intensities are (see Del Zanna et al. 2004 for details).

4.1. $3s^2\,3p^6\,3d^2$–$3s^2\,3p^5\,3d^3$ transitions

The emissivity ratio curves for the stronger lines are given in Fig. 4, while those for the weaker ones in Fig. 5. The same normalization factor was used.

The strongest line (3−135) is the main decay from a highly-mixed level, with a dominant component originating from the ^3F term. It was correctly identified by FC73, together with the two other main decays from levels originating from the same term, the 2−133 and 1−131 transitions, among the top brightest lines. There is excellent agreement between predicted and observed intensities of these three transitions, once blending is taken into account. The 2−133 176.927 Å line is blended with a strong Fe IX line, while the 1−131 177.171 Å with a strong well-known Fe X (Del Zanna et al. 2004).

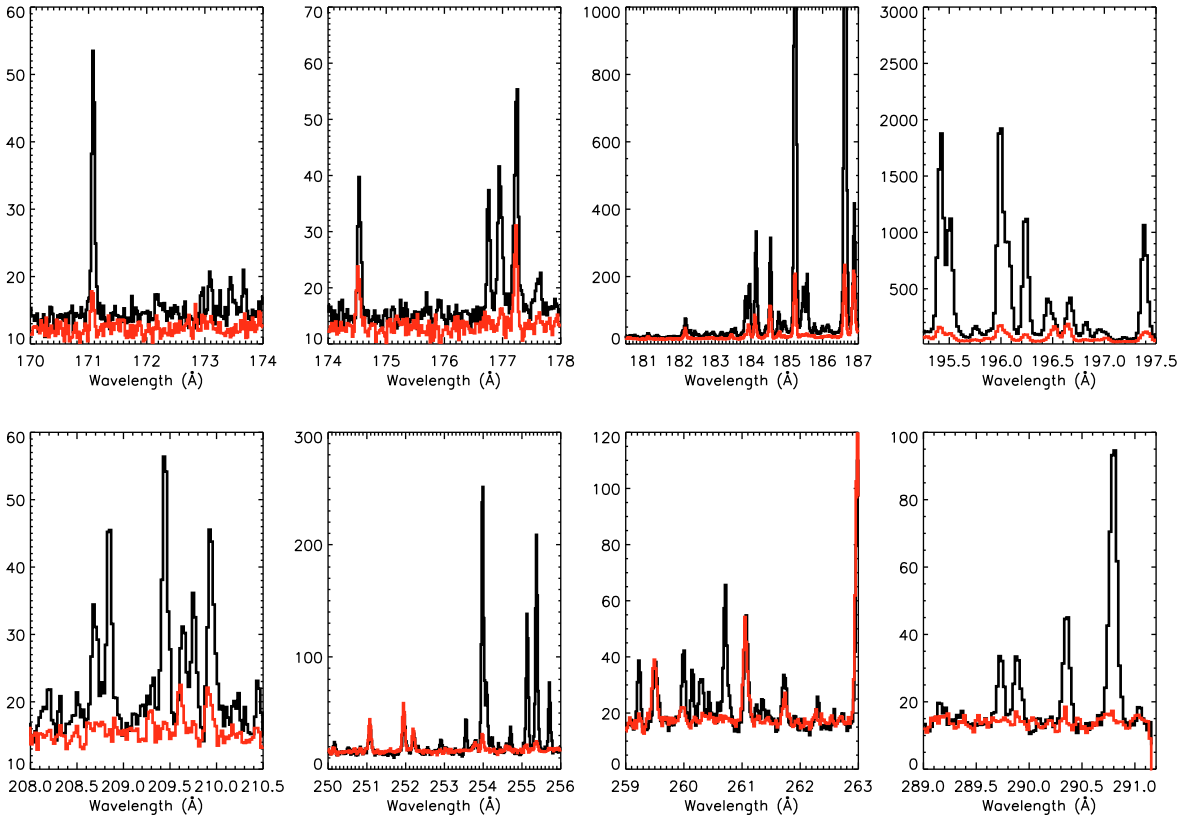

Fig. 3. Hinode EIS spectra (units are averaged counts per pixel) relative to two different areas. Thick lines refer to the spectrum over the sunspot leg, where transition region lines are much enhanced. The thick red line shows the foreground sunspot spectrum.

The second strongest line (3−148) was also correctly identified by FC73, together with the other main decay from a level originating from the same ^3D term (2−147).

The third brightest transition (8−150) was identified by E81 with a line observed at 173.442 Å, and 2 coincidences. The identification of this decay from the $^1G_4$ is inconsistent with the atomic data and the observations. Hinode observed a TR line which could be this transition, but with a lower intensity than predicted, and a wavelength of 173.434 Å. The predicted intensity is on firm grounds. The benchmark calculation confirms the gf value of WB08, indeed the level is not highly mixed. FC73 did suggest an alternative identification, a line observed at 167.6 Å (not observed by E81). However, the energy of the $^1G_4$ would be very far from the predicted one. It is possible that the identification of this strong line has been hindered by blending with another strong line. We give a tentative suggestion that it is the strong Fe IX 171.077 Å.

The identification from E81 of the fourth strongest transition (3−110) with the 195.388 Å line must also be incorrect, on various grounds. Firstly, the 195.388 Å line has a morphology close to Fe VIII, and not Fe VII, as Fig. 1 shows. Secondly, the predicted intensity does not match the observed one. Thirdly, the predicted energy splitting between level 110 and those mainly originating from the ^3G term is inconsistent with the energies of levels 108 and 106. Level 110 is very mixed, however the benchmark calculation gives $gf = 2.9$, close to 2.99, the value pertinent to the scattering calculation, hence the predicted intensity of the 3−110 line should be accurate. The main decay from level 108 (2−108) was identified by E81 with the 196.243 Å line, while the main decay of the (relatively pure) 106 level ($^3G_3$) was identified by E81 with the 196.045 Å line. The benchmark calculation gives a gf value for the 1−106 transition in good agreement with that from WB08, while a lower value is found for the 2−108 transition. The same calculation also suggests, based on the predicted splittings between these levels, that the three transitions 3−110, 2−108, 1−106 should be identified with the lines observed by Hinode EIS at 196.043, 196.209, 197.364 Å respectively. Notice that E81 identified the 196.045 Å line with the 1−106 transition instead. The predicted intensities for these three lines are in excellent agreement with the observed ones, as shown in Fig. 4. Notice that the 196.209 Å is a self-blend, and the 197.364 Å is blended with a strong Fe VIII line (see Del Zanna 2009). The previous identifications, on the other hand, are inconsistent with the atomic data, as Fig. 4 shows.

E81 did not identify the 8−153 transition, predicted to be the fifth strongest, and that one which has the largest gf value of all the EUV lines. Level 153 is highly mixed, however the benchmark calculation suggests that a value of $gf = 10$ is correct. The only plausible explanation for E81 not having identified the strongest line is that it was blended in the spectrum. The only reasonable candidate from E81's list is the strong 165.087 Å line, blended with the 2−147 transition, possibly still blended with the weak 9−177 ($gf = 1.7$) transition, which was the original identification.

The next strongest line was not identified by E81. It is the main decay from the $^1H_5$ (8−116). The level is not highly mixed and the predicted intensity should be accurate. This line must be strong in the EIS spectrum. It is identified here with the 196.209 Å self-blend, on wavelength and intensity grounds.

Levels 19 and 20 were not identified by E81, despite producing transitions of equal strength (3−19, 3−20). Given their strength, these lines ought to be well observable by EIS. A search

Table 3. List of measured transition-region emission lines from the foreground-subtracted spectrum of the sunspot loop.

λ_o	λ_c	DN	Int	F	ID
171.083	.077	101.7	1362.8	67	Fe IX (bl Fe VII?)
173.088		16.6	52.4	55	O VI (sbl) 173.079
173.451	173.434	19.9	57.	63	? Fe VII
174.536	.533	37.7	84.6	57	Fe X 174.534
176.761	.743	58.6	55.1	55	Fe VII
176.950		87.3	73.6	70	Fe VII + Fe IX
177.226	.208	86.8	65.1	70	N Fe X +Fe VII
180.382		122.3	26.9	55	u (bl Fe X)
181.103		30.2	5.1	70	u (bl Fe XI)
182.151		99.7	11.9	70	N Fe VII (bl Fe XI oc)
182.289		70.2	8.0	70	u (bl Fe X)
183.557		90.6	7.0	70	u
183.841	.823	363.1	25.8	70	Fe VII (bl Ni VIII?)
183.953	.935	416.8	28.6	70	O VI 183.937 (bl)
184.140	.121	774.1	50.5	70	O VI (bl Ni VIII?)
184.420		82.4	4.9	70	u
184.533	.530	555.1	32.2	55	Fe X (bl ?) 184.543
184.769		161.5	8.8	68	u (bl Fe XI)
184.924		135.4	7.2	70	u
185.226	.214	8009	390.6	63	Fe VIII (bl oc)
185.458	.445	440.7	20.3	70	Mn VIII 185.46
185.560	.542	403.6	18.1	55	Fe VII
185.593		124.8	5.4	70	u
185.776		94.3	4.0	70	u
185.991		89.2	3.6	70	u
186.131		112.7	4.4	70	u
186.619	.607	8218	291.9	70	N Fe VIII (bl Fe VII,oc)
186.870	.852	571.0	19.2	70	N Fe VII (bl Fe XII oc)
187.255	.243	1049	32.6	64	Fe VIII 187.237
187.707		291.3	8.4	70	u VII?
187.972		375.8	10.3	70	u (bl oc)
188.188	.170	753.7	19.7	70	N Fe VII (bl Fe XI oc)
188.417		735.0	18.7	55	Fe VII (bl Mn IX)
188.499	.493	1693	42.3	60	Fe IX
188.591	.572	736.2	18.2	60	u VII
188.646	.640	163.7	4.0	70	T N Fe IX
188.813		274.4	6.5	70	u
189.350	.331	453.8	10.0	70	u VII
189.473	.454	875.3	19.0	65	Fe VII
189.942	.935	1358	27.5	67	Fe IX
190.035		704.1	14.1	70	Fe X (bl u) 190.038
190.897	.891	304.8	5.5	70	T N Fe IX
191.040		212.6	3.8	70	u (bl oc)
191.213	.206	914.7	15.9	58	Fe IX (bl)
191.392		267.8	4.6	70	u (bl oc)
191.598		613.9	10.3	70	Mn IX 191.570
191.781		307.4	5.0	70	u (bl oc)
192.013		1265.2	20.3	70	u (bl Fe VIII oc)
192.099		636.4	10.1	63	u IX?
192.635		754.0	11.5	70	u (bl Fe XI)
192.801	.782	1765.3	26.5	70	O V (sbl)
192.926	.907	2568.2	38.2	64	O V (sbl)
193.256		256.6	3.7	55	u
193.718		526.2	7.4	70	u (bl Fe X)
193.830		184.0	2.6	57	u (bl oc)
193.985	.972	797.0	11.1	55	Fe VIII 193.968
194.286		150.6	2.1	70	u
194.370		89.0	1.2	55	? Mn X 194.34
194.671	.658	7963.6	107.1	63	Fe VIII 194.660
194.791	.784	1334.4	17.9	70	N Fe IX
195.406	.393	5293.6	70.0	65	u VIII
195.490	.471	2605.4	34.4	55	u VII
195.750		409.1	5.4	70	T N Fe IX
195.982	.969	5573.1	73.7	64	Fe VIII 195.972

Table 3. continued.

λ_o	λ_c	DN	Int	F	ID
196.063	.043	2537.2	33.6	70	N Fe VII 196.046
196.229	.209	3356.3	44.5	65	N Fe VII (sbl) 196.210
196.445	.425	1188.3	15.9	70	u VII
196.662	.649	837.0	11.3	70	Fe VIII (bl u Fe XII oc)
196.809		500.8	6.8	70	u
196.935		300.6	4.1	70	u
197.377	.364	3064.0	43.2	69	N Fe VIII (bl Fe VII)
197.861	.854	1207.2	17.9	70	N Fe IX
198.079		116.0	1.8	70	u
198.248	.228	291.4	4.6	70	u VII
198.388		229.2	3.7	70	u
198.557		635.0	10.5	70	? S VIII 198.550
199.325		154.2	3.0	70	Mn IX 199.320
199.605	.602	241.0	5.1	70	u X
199.791		76.9	1.7	70	u
200.160	.146	259.6	6.4	66	u VIII
200.385		71.7	1.9	70	u
200.670		114.5	3.4	70	u
200.781	.767	302.8	9.2	70	u VIII
200.999		111.3	3.7	70	? Cr VI (bl oc)
201.480		81.9	3.3	70	? Cr VI
201.612		237.6	10.0	70	u VII? (bl)
201.714		57.1	2.5	55	u (bl Fe XI)
201.876	.856	327.3	15.4	63	Fe VII? (bl)
202.393		152.8	9.0	70	u
202.604		94.6	6.0	70	? S VIII 202.608
202.847	.827	915.0	63.7	67	Cr VII 202.83
204.718	.704	492.2	59.9	66	Fe VIII
204.893		61.8	7.9	55	u (bl oc)
205.053	.046	199.3	26.1	64	Cr VIII 205.04
205.722	.716	88.4	13.3	63	Cr VIII 205.72
206.775	.754	88.7	16.2	60	N Fe VII
207.138	.124	262.0	50.8	70	Fe VIII
207.217		73.5	14.5	70	u VI?
207.457		48.3	9.9	67	u (bl Fe X)
207.739		135.4	29.1	66	u VI ?
208.687	.680	51.9	13.4	66	? Cr VIII 208.63
208.844	.823	88.3	23.4	62	N Fe VII
209.440		124.9	36.8	70	u VI ?
209.647		27.1	8.3	70	u (bl oc)
209.751	.731	48.7	15.3	60	N Fe VII
209.940		72.9	23.7	70	u (bl oc)
246.027	.002	966.6	201.5	74	Si VI (bl Fe VII) 246.000
248.489	.460	285.3	50.5	69	O V 248.490
248.659		67.1	11.8	56	u VI?
249.152	.127	525.0	90.2	58	Si VI (bl oc)
249.310		114.2	19.5	55	u
252.906		32.1	3.9	80	u
253.546	.520	76.7	8.9	55	T N Fe VII
253.973	.956	695.5	78.4	64	Fe VIII (bl S X)
254.076	.051	184.5	20.6	66	N Fe VII (sbl, bl u)
254.209		35.2	3.9	58	u
254.702		46.4	4.9	55	u
255.127	.110	355.0	36.7	68	Fe VIII (bl)
255.363	.346	530.3	53.6	62	Fe VIII
255.701	.684	163.1	16.1	61	Fe VIII
257.265	.261	291.3	25.8	55	Fe X 257.262
259.214		58.9	4.6	55	? Cr VII
259.982		58.8	4.4	55	u X?
260.133	.107	54.4	4.0	55	Fe VII
260.284		51.0	3.7	63	u
260.702	.676	153.4	11.0	77	N Fe VII
261.700		35.8	2.4	60	u
262.296		13.5	0.9	55	u VII ?
262.947		42.8	2.7	55	u (bl Fe XVI oc)

Table 3. continued.

λ_o	λ_c	DN	Int	F	ID
265.729		80.8	4.5	57	u
266.205		69.0	3.8	80	u VII?
266.419		66.0	3.6	80	u (bl Fe XVII oc)
266.542		61.0	3.3	73	u
266.620		60.5	3.3	60	u (tr) 266.630
266.991		31.0	1.7	73	O IV
267.229		108.1	5.7	64	u VII?
267.292		202.7	10.7	68	u V?
268.042		52.2	2.7	80	u VII?
268.220		46.1	2.4	68	u
269.014	.987	2419.7	122.5	74	Mg VI 268.991
270.419	.392	5058.0	254.0	71	Mg VI 270.391
271.049		148.6	7.5	80	O V (bl)
271.714		241.2	12.3	74	u VII?
272.161		118.6	6.1	80	u
272.329		93.1	4.8	80	u
272.679	.661	1089.2	56.8	70	Si VII 272.638
274.192	.174	498.3	27.7	55	Si VII (bl Fe XIV oc)
275.388	.370	3068.2	182.3	72	Si VII 275.350
275.704	.686	520.7	31.6	73	Si VII 275.670
276.163	.145	516.5	32.5	67	Mg VII 276.145
276.613	.581	1940.3	126.2	74	Mg V 276.581
276.874		850.5	56.5	72	Si VIII+VII (bl u)
277.022		1846.8	124.4	88	Mg VII (bl Si VIII)
278.430	.411	2924.7	223.9	98	Mg VII (bl Si VII) 278.395
278.727		179.3	14.2	77	? Al V (bl) 278.694
279.656		46.8	4.1	55	O IV (bl)
279.970	.937	183.9	16.6	65	O IV 279.930
280.751	.732	763.0	75.1	71	Mg VII (bl ?) 280.737
281.430		32.4	3.4	55	? Al V 281.394
289.713	.684	57.1	15.4	55	N Fe VII 289.678
289.867	.838	64.5	17.7	73	N Fe VII 289.831
290.332	.303	108.4	31.5	79	N Fe VII 290.307
290.777	.748	312.2	95.8	80	N Fe VII 290.750

Note: λ_o (Å) is the measured wavelength. λ_c (Å) is the measured wavelength corrected for the red-shift. Lines from Fe X have been corrected for 5 km s^{-1}, those from Fe IX and Cr VIII for 10 km s^{-1}, those from Fe VIII, Si VII, Mg VII, Mn VIII for 20 km s^{-1}, while those from Fe VII, Si VI, Mg VI, Cr VII for 30 km s^{-1}. The few lines from Mg V, O V, O IV for 35 km s^{-1}. DN is the number of total counts in the line, while Int is the calibrated intensity (phot cm^{-2} s^{-1} arcsec^{-2}). F is the full-width-half-maximum in mÅ, while the column ID provides the identification (bl: blended; sbl: self-blend; u: unidentified; bl oc: blended in other plasma conditions). In a few cases, the class of a line is given (i.e.: u VII is a line with a morphology similar to Fe VII), as well as the rest wavelength (Å) from the literature. "N" indicates a new identification proposed here, while "T N" a tentative new one.

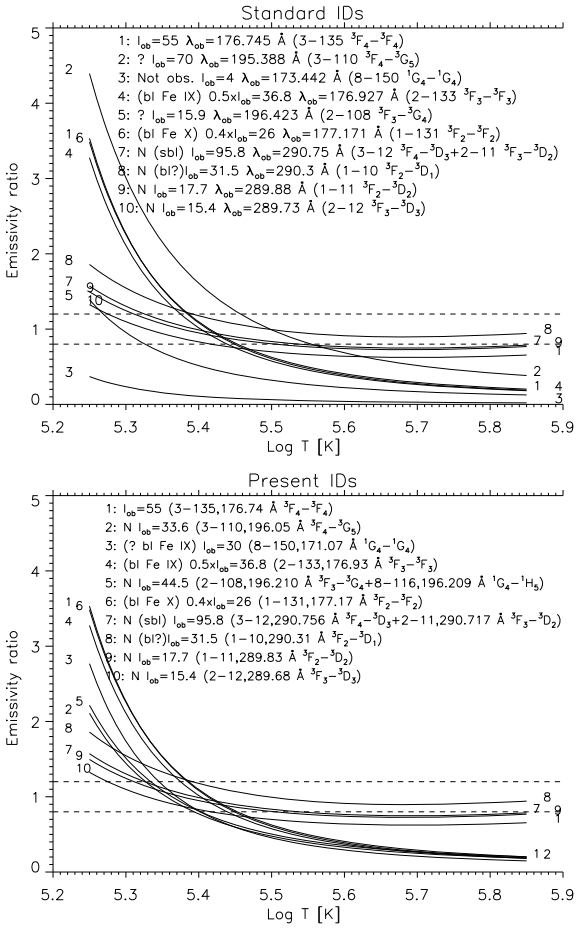

Fig. 4. The emissivity ratio curves relative to some of the strongest Fe VII EUV transitions observed in the "foreground-subtracted" sunspot loop leg by Hinode EIS. The curves were calculated at log N_e [cm^{-3}] = 9. I_{ob}: observed intensity; bl: blend; sbl: self-blend; N: new identification proposed here. *Top*: using the previous identifications from E81. *Bottom*: using the present identifications.

through the reasonable spectral region suggest that these two lines are observed at 260.676 and 254.051 Å. No other possibilities were found. The 254.051 Å line is too strong to be blended with either of the Fe VIII 253.95, 255.101 Å lines (Del Zanna 2009).

The following levels have a slightly more uncertain identification. Level 118 ($^3D_2$) was identified by E81 with 4 coincidences, the strongest transition being the 6−118, identified with a line observed at 189.450 Å. The predicted intensity is weaker than the observed one from Hinode EIS, however this could be due to blending with another TR line. If this identification is correct, this means that the positioning of the ^3D term is known. The main other level, very mixed, originating from this term is level 119. The main transition is the 4-119, identified by E81 at 185.547 Å. Morphology and intensity measured from Hinode EIS are in good agreement with the predicted one, however the splitting of the ^3D term predicts a wavelength 2.5 Å away. An alternative suggestion, which gives TEC in agreement with the others, the correct splitting and the correct intensity is given instead: the 4−119 is blended with the Fe XII self-blend (first identified by Del Zanna & Mason 2005). This self-blend is of particular importance because is one of the main density diagnostics for EIS. The 6−118 is identified with a self-blend observed at 188.18 Å, and normally blended with various other transitions, the main one being from Fe XI (Del Zanna et al. 2009).

The 7−134 line, identified by E81 at 183.825 Å using four coincidences, is twice as strong as predicted, in the EIS spectra. An alternative, which gives good TEC agreement and good match in intensity is the 182.133 Å line, normally blended with an Fe XI transition.

The 4−121 line was identified by E81 at 186.656 Å. This line would be blended with a much stronger Fe VIII transition. Again, TEC and intensity arguments suggest that this transition is the 183.823 Å line instead.

The mixed levels 97, 98, 101, originating from a ^3G term, produce the 1−101, 3−97, 2−98 transitions, all of similar strengths and observable by EIS. The identifications proposed by E81 (211.931, 212.663, 207.712 Å) cannot be reconciled

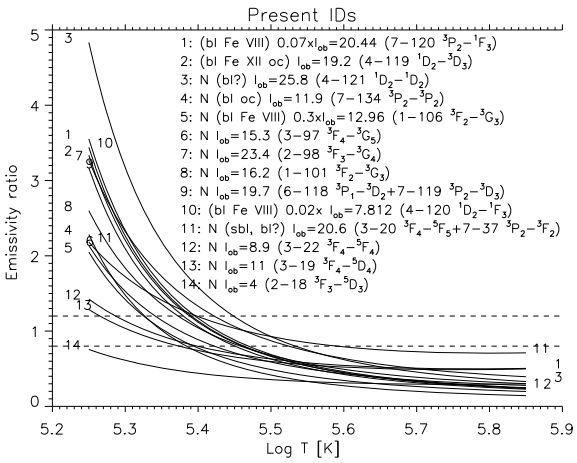

Fig. 5. The emissivity ratio curves relative to some of the weaker Fe VII EUV transitions observed by Hinode EIS. The curves were calculated at log N_e [cm^{-3}] = 9.

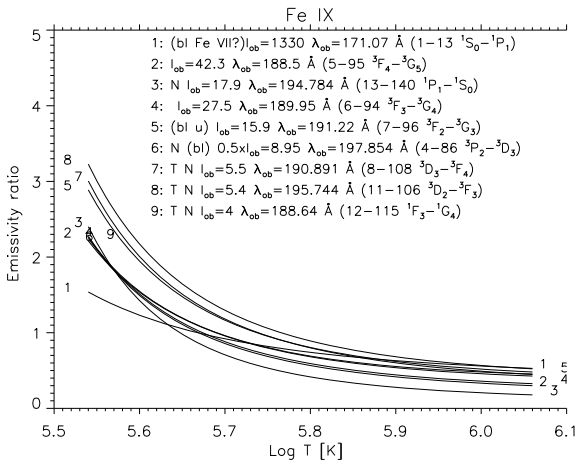

Fig. 6. The emissivity ratio curves relative to the Fe IX EUV transitions observed by Hinode EIS calculated at log N_e [cm^{-3}] = 9. N are new identifications, while T N are tentative new ones.

with the predicted splittings. A good match in both wavelengths and intensities is found for the three lines observed at 206.754, 209.731, 208.823 Å. The 212.664 Å line was observed by EIS, but is assigned to the 3–93 transition, again on wavelength and intensity grounds.

4.2. $3s^2\ 3p^6\ 3d^2$–$3s^2\ 3p^6\ 3d\ 4p$ transitions

These transitions fall around 240 Å and are not observable by Hinode EIS, however all the identifications proposed by E81 appear correct. All levels have similar TEC, and all observed energy splittings are in good agreement with theory.

4.3. $3s^2\ 3p^6\ 3d^2$–$3s^2\ 3p^6\ 3d\ 4s$ transitions

The few decays from the $3s^2\ 3p^6\ 3d\ 4s$ configuration are of particular importance because they offer a good temperature diagnostic, when observed with the decays from the much higher 3d or 4p levels. The energies of the $3s^2\ 3p^6\ 3d\ 4s$ levels were obtained by E81 indirectly, from various UV lines of the transition array 3d 4s–3d 4p, and knowing the energies of the 3d 4p levels. For the first time, EIS has observed these decays. The lines are not very strong because they are near the edge of the detector, where the sensitivity is low, however are well observed. Their wavelengths are in very good agreement (within uncertainty) with the values predicted by E81. The 1–10 is observed at 290.303, rather than 290.307 Å. The 1–11 at 289.838 Å, instead of 289.831 Å. The 3–12 is blended with the 2–11, which should be at 290.724 Å. E81's energies predict a wavelength of 290.756 Å for the 3–12 line, in good agreement with the observed blend at 290.748 Å.

5. Benchmarking other ions

For the following benchmark the atomic data in CHIANTI v.5.2 (Landi et al. 2006) were used.

5.1. Fe IX

The emissivity ratio curves relative to the Fe IX EUV transitions observed by Hinode EIS are shown in Fig. 6. The strongest is the resonance 1–13 171.07 Å line, which is the strongest EUV line in quiet Sun conditions. For EIS, this line is close to the edge, where the sensitivity is low, so long exposures are required to obtain a good measurement of the line. Young (2009) used the atomic data produced by Storey et al. (2002) (present in CHIANTI v.5) to identify four new lines from the $3s^2\ 3p^4\ 3d^2$ configuration. The three main decays from the $^3G_{4,5,3}$ were identified with the lines observed at 189.941, 188.497, 191.216 Å. These identifications are confirmed on intensity and wavelength grounds. As shown by Young (2009), the combination of one of these lines with the resonance line provides an electron temperature diagnostic. A value of log T[K] = 5.65 is obtained, which is significantly lower than the temperature of maximum abundance in ionization equilibrium. The sensitivity, however, is not very high, and a broad range of temperatures are consistent with the data. Further, the accuracy of the EIS ground radiometric calibration (used here) toward the edge at 171.07 Å is difficult to assess.

The main decay from the $^3D_3$ (4–86) is predicted to be a line well-visible by EIS. The energy difference between ab-initio energies and those of the $^3D_3$ predict that the 4–86 line should fall around 197.2 Å. The only line with the appropriate morphology is a line observed at 197.854 Å. There is excellent agreement between the predicted and observed intensity. The same line was instead identified by Young (2009) with the main decay from the $3s^2\ 3p^5\ 4p$ (13–140), observed at 197.862 Å. There are no other observed levels from the $3s^2\ 3p^5\ 4p$ configuration, so it is not easy to identify any lines originating from this configuration. If we assume for the $3s^2\ 3p^5\ 4p$ the same correction as for the $3s^2\ 3p^4\ 3d^2$ to the ab-initio energies, we can estimate that the 13-140 transition should fall around 187 Å. The only viable candidate on intensity grounds is the line observed at 194.784 Å, which would be blended.

Using the same energy corrections, three further weaker transitions from the $3s^2\ 3p^4\ 3d^2$ configuration have been identified. These identifications should be treated as tentative, however excellent agreement between observed and predicted intensities is present as Fig. 6 shows.

5.2. Fe X

The emissivity ratio curves relative to the Fe X EUV transitions observed by Hinode EIS are shown in Fig. 7. The identifications

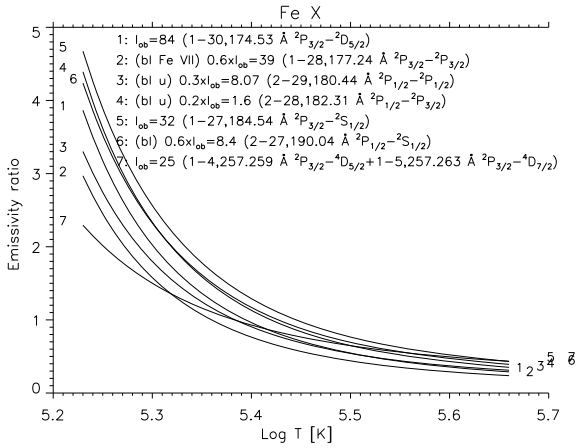

Fig. 7. The emissivity ratio curves relative to the Fe X EUV transitions observed by Hinode EIS calculated at log N_e [cm^{-3}] = 9.

and the atomic data for these lines is presented in Del Zanna et al. (2004). It is interesting to notice that the three strongest transitions (1−30 at 174.53 Å, 1−28 at 177.24 Å blended with Fe VII, and the self-blend 257.26 Å line) have observed intensities in very good agreement with theory, and consistent with an isothermal plasma at log T[K] = 5.4. However, this result is very uncertain, considering that temperature sensitivity is not very high, as it was the case for Fe IX. Also, that there is a density dependence in the 257.26 Å line above log N_e = 9. The other weaker lines appear to be blended in this spectrum.

5.3. Si VII and Mg VII

The emissivity ratio curves relative to the Si VII and Mg VII EUV transitions observed by Hinode EIS are shown in Fig. 8. They were calculated at log T [K]= 5.8, however there is no temperature dependence for the lines considered here. The 2−8 line from Si VII is normally blended with a strong Fe XIV transition. The foreground subtraction leaves an intensity for the line which provides a measurement of the electron density of log Ne = 8.8. Via a branching ratio, it is possible to estimate quite accurately, using the strong 1−6 transition, the intensity of the 2−6 line, which blends the Mg VII 3−14 line, which is an important density diagnostic for the EIS spectral range. This line gives a density of log Ne = 9.5, when used in conjunction with the strong 4−15 line. There is disagreement with the Si VII measurement. The Mg VII branching ratio suggests that the 2−14 transitions should be 80% the intensity of the blend with Si VIII observed at 277. Å. There is another transition from Si VIII, observed at 276.85 Å, this time blended with the Si VII 276.84 Å, which intensity can be estimated accurately via another branching ratio with the strong 272.64 Å. The model for Si VIII however provides a disagreement of a factor of 2 between the two lines. This could be ascribed to a further TR line blending at 276.84 Å. In summary, more work needs to be done to properly assess Si VII and Mg VII lines before they can be used reliably.

5.4. O VI and O V

The emissivity ratio curves relative to the O VI and O V EUV transitions observed by Hinode EIS are shown in Fig. 9. The density obtained from the O V lines is very close to what expected. Excellent agreement is found between observed and predicted intensities. This rules out the possibility

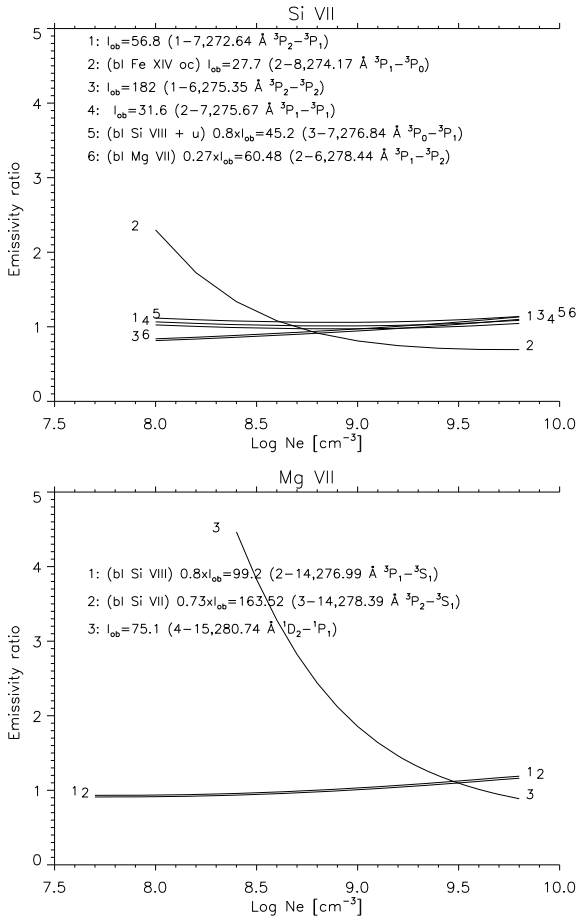

Fig. 8. The emissivity ratio curves relative to the Si VII and Mg VII EUV transitions observed by Hinode EIS, calculated at log T[K] = 5.8.

of blending with other TR lines. This is an important issue for the 192.8 Å blend, where the Ca XVII resonance line and at least two other Fe XI lines are present. This is because the Ca XVII is the strongest line in an important temperature range, and efforts are on-going to estimate the Ca XVII from the observed blend (see, e.g. O'Dwyer et al. 2009).

5.5. Other ions

The strongest transitions from Cr VI, Cr VII, Cr VIII, Mn VII, Mn VIII, Mn IX, were identified by Gabriel et al. (1965) and are also observed in the EIS spectra.

6. Summary and conclusions

Spatially-resolved high-resolution solar spectroscopy is very valuable for line identification purposes. After very careful data analysis, Hinode EIS spectra can provide very accurate wavelengths (down to a few m Å) and line intensities. The overall benchmark of atomic data using a spectrum emitted at transition-region temperatures is very satisfactory. Most of the strong lines in the spectrum have been identified, and have good agreement (within 20%) between expected and observed intensities. Some wavelengths have been revised. However, a number of strong transitions still await firm identifications. Work is in progress to improve some of the atomic models for some ions. The fact that many lines are blended has been highlighted. Notice, however,

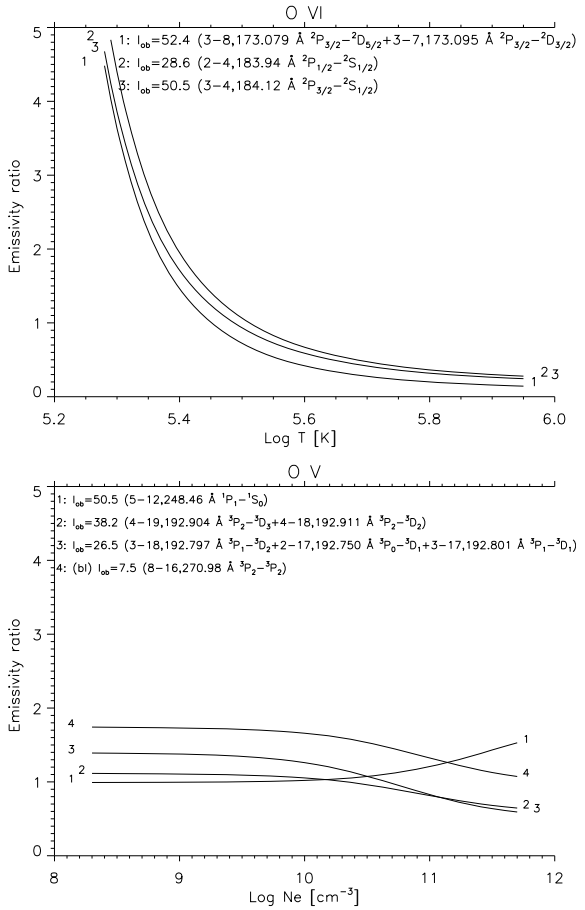

Fig. 9. The emissivity ratio curves relative to the O VI and O V EUV transitions observed by Hinode EIS.

that only blending with cool lines was considered here. Blending in other conditions is described in a follow-up paper.

A series of inconsistencies in the (otherwise excellent) work of Ekberg (1981) on Fe VII were found. The large-scale electron scattering calculation of Witthoeft & Badnell (2008) appears to be very accurate, so the inconsistencies in Ekberg's work could only be ascribed to mis-identifications. Further experimental data will be needed to confirm many of the identifications of the weaker lines that have been proposed here. Identifications along the sequence are being revisited.

A few important temperature diagnostics for the solar transition region and independent from the assumption of ionization equilibrium have been highlighted here. All the temperature diagnostics are consistent with loop legs close to being isothermal but at temperatures well below the peak ion abundance in ionization equilibrium for ions formed at upper transition region temperatures such as Fe VIII (Del Zanna 2009), Fe IX, Fe X. This is not surprising, considering that loops are radiatively-cooling structures of down-flowing plasma (Del Zanna 2008; Bradshaw 2008). A full study of this issue is the subject of a follow-up paper.

Acknowledgements. Support from STFC (Advanced Fellowship and APAP network) is acknowledged.
I warmly thank B.C. Fawcett for helping in identify some of the best plates of his archive.
The analysis of this Hinode/EIS observation was stimulated by the participation to the Coronal Loop Workshop held in Santorini in June 2007 and by various communications with M. Witthoeft.
The excellent Hinode Science Data Centre Europe was used to search the EIS database.
Hinode is a Japanese mission developed and launched by ISAS/JAXA, with NAOJ as domestic partner and NASA and STFC (UK) as international partners. It is operated by these agencies in co-operation with ESA and NSC (Norway).

References

Badnell, N. R. 1997, J. Phys. B Atomic Mol. Phys., 30, 1
Bradshaw, S. J. 2008, A&A, 486, L5
Culhane, J. L., Harra, L. K., James, A. M., et al. 2007, Sol. Phys., 60
Del Zanna, G. 2007, in ASPC, First Science results from Hinode, 397, 87
Del Zanna, G. 2008, A&A, 481, L49
Del Zanna, G. 2009, A&A, 508, 513
Del Zanna, G., & Mason, H. E. 2003, A&A, 406, 1089
Del Zanna, G., & Mason, H. E. 2005, A&A, 433, 731
Del Zanna, G., Berrington, K. A., & Mason, H. E. 2004, A&A, 422, 731
Del Zanna, G., Storey, P. J., & Mason, H. E. 2009, A&A, accepted
Dere, K. P., Landi, E., Mason, H. E., Monsignori Fossi, B. C., & Young, P. R. 1997, A&AS, 125, 149
Dere, K. P., Landi, E., Young, P. R., et al. 2009, A&A, 498, 915
Ekberg, J. O. 1981, Phys. Scr., 23, 7
Ekberg, J. O., & Feldman, U. 2003, ApJS, 148, 567
Fawcett, B. C., & Cowan, R. D. 1973, Sol. Phys., 31, 339
Gabriel, A. H., Fawcett, B. C., & Jordan, C. 1965, Nature, 206, 390
Haugan, S. V. H. 1997, SOHO CDS software note, 47
Ishikawa, Y., & Vilkas, M. J. 2008, Phys. Rev. A, 78, 042501
Landi, E., Del Zanna, G., Young, P. R., et al. 2006, ApJS, 162, 261
Nussbaumer, H., & Storey, P. J. 1978, A&A, 64, 139
O'Dwyer, B., Del Zanna, G., Mason, H. E., et al. 2009, A&A, submitted
Storey, P. J., Zeippen, C. J., & Le Dourneuf, M. 2002, A&A, 394, 753
Witthoeft, M. C., & Badnell, N. R. 2008, A&A, 481, 543
Young, P. R. 2009, ApJ, 691, L77
Zeippen, C. J., Seaton, M. J., & Morton, D. C. 1977, MNRAS, 181, 527